Random three-dimensional jammed packings of elastic shells acting as force sensors

Jissy Jose,[*] Alfons van Blaaderen,[†] and Arnout Imhof[‡]

Soft Condensed Matter, Debye Institute for NanoMaterials Science, Utrecht University, Princetonplein 1,
3584 CC, Utrecht, The Netherlands

In a jammed solid of granular particles, the applied stress is in-homogeneously distributed within the packing. A full experimental characterization requires measurement of all the interparticle forces, but so far such measurements are limited to a few systems in two and even fewer in three dimensions. Particles with the topology of (elastic) shells are good local force sensors as relatively large deformations of the shells result from relatively small forces. We recently introduced such fluorescent shells as a model granular system in which force distributions can be determined in three dimensions using confocal microscopy and quantitative image analysis. An interesting aspect about these shells that differentiates them from other soft deformable particles is their buckling behavior at higher compression. This leads to deformations that do not conserve the inner volume of the particle. Here we use this system to accurately measure the contact forces in a three-dimensional packing of shells subjected to a static anisotropic compression and to shear. At small deformations forces are linear, however, for a buckled contact, the restoring force is related to the amount of deformation by a square root law, as follows from the theory of elasticity of shells. Near the unjamming-jamming transition (point J), we found the probability distribution of the interparticle forces $P(f)$ to decay nearly exponentially at large forces, with little evidence of long-range force chains in the packings. As the packing density is increased, the tail of the distribution was found to crossover to a Gaussian, in line with other experimental and simulation studies. Under a small shear strain, up to 0.216, applied at an extremely low shear rate, we observed a shear-induced anisotropy in both the pair correlation function and contact force network; however, no appreciable change was seen in the number of contacts per particle.

I. INTRODUCTION

One of the key features that defines a jammed state of granular and colloidal particles is the force network that spans the system. This random network of contact forces imparts rigidity to a jammed packing that hence acts like a solid, with several anomalous properties not found with other elastic solids such as crystals. The most simple and widely used quantitative way to characterize a force network is to measure the probability distribution of the interparticle forces, $P(f)$ [1–3]. Most published force distributions have been determined in simulation and theoretical studies, and only a few experimental systems are presently known for which these contact forces could be accurately measured, either in two or especially three dimensions. In addition, experimental work on three-dimensional (3D) jamming behavior is scarce, owing to a lack of availability of tools, techniques, and model systems with which dense packings can be studied quantitatively on the single particle level, including a quantitative description of all the forces between the particles.

Experimental studies on contact force networks started in granular materials research with measurements of forces exerted by the grains against a constraining surface using a carbon-paper technique [1,4–6]. In this technique all constraining surfaces of the system were lined with a layer of carbon paper covering a white paper. Grains pressed the carbon onto the white paper and left marks at the contact regions whose

size and intensity depends on the magnitude of the normal force on the corresponding grain. By using image analysis software and calibration curves, the contact forces at the surface were extracted. However, this method lacks precision and information about force transmission in the bulk. A more precise method to measure boundary forces was introduced by Løvoll *et al.* [7], using a high-precision electronic balance. In addition to boundary forces, interparticle force analysis in the bulk has been achieved, enabling an investigation of the relations between the geometry of the packing and the spatial structure of the force network [1,8]. Majmudar *et al.* [8] measured the normal and tangential forces inside a two-dimensional (2D) system of bidisperse photoelastic disks that were subjected to pure shear and isotropic compression. The stress-induced birefringence of the disks also allowed *in situ* visualization of force chains in their system. The system under stress was imaged through crossed polarizers. From the images contact forces were obtained by fitting the observed photoelastic patterns inside each disk to the 2D elasticity solution [9] for the stress inside a disk. Although this system is one of the first experimental systems for which quantitative forces could be measured, the deformation per disks was less than 1% of the average diameter in the compressed state [10], which prevented the study of higher volume fractions, significantly beyond the jamming point with this model system and methodology.

Systems that can reach high volume fractions close to unity are those comprised of softer deformable particles, for example, emulsions and foams [11–15]. Katgert *et al.* extracted various statistical and geometrical quantities in a 2D static packing of foam bubbles through image analysis. Brujic *et al.* [12,13] introduced, as far as we are aware for the first

---

[*]jissyjose10@gmail.com
[†]A.vanBlaaderen@uu.nl
[‡]A.Imhof@uu.nl

time, a method for measuring the contact force distribution within the bulk of a 3D compressed emulsion system using confocal microscopy. The oil droplets were index matched and fluorescently labeled. Using image analysis routines based on a Fourier filtering method the positions and radii of the polydisperse emulsion droplets were extracted and the spheres were reconstructed. By analyzing either the size of the contact area or the enhanced fluorescence intensity at contact regions, the degree of deformation and hence the interdroplet normal forces were calculated. 3D confocal microscopy was also used by Zhou *et al.* [14] in 3D piles of frictionless liquid droplets labeled with a monolayer of fluorescent nanoparticles and Caswell *et al.* [16] in a dense 3D packing of soft colloids made of poly N-isopropyl acrylamide (pNIPAM) to obtain 3D images.

The probability distribution of interparticle forces $P(f)$ from these studies is a broad distribution with an exponential like tail and a peak or a plateau below the average force [1,3–6,8,11–15,17–20]. Moreover, in some studies the exponential tail is found to crossover to a Gaussian for an increase in the degree of deformation of the particles or for packing densities well above the jamming transition [11,12,14,21,22], but it is still not clear at what point it starts to behave like a homogeneous, elastic solid block. Thus the majority of contacts in a marginally jammed solid bear forces smaller than the average, and there are only a few contacts that carry large forces, which were found to form chainlike structures [1,3,8,14,15,23]. Studies have shown an anisotropy in the force network, where the chains oriented in a preferred direction under a globally applied shear [8,24–28].

Because we feel it is important that there are more granular model systems available with different properties from those already studied to be able to check generality of the findings so far, we recently introduced a granular model system. This system is suitable to study forces in packings, and it comprises fluorescently labeled elastic shells that interact through short-ranged repulsive forces [29]. These charged spherical particles (with a size around 5 μm, although we recently were successful in also creating monodisperse droplets with larger size even further into the granular regime [30]) contain a solid membrane with a liquid interior [30]. The membrane is a cross-linked network formed from a mixture of silicone and silica forming monomers and with a Young's modulus of 200 MPa [31]. A key feature of these particles is the membrane elasticity, which facilitates reversible deformations, as shown in our recent articles [29,32]. Therefore they can serve as a sensor of local force. Additionally, there are possibilities to tune several features of these particles, for example, friction, mechanical properties, permeability and shape, which are highly relevant in jamming research as particle-level properties control the behavior in a jammed state [33–35]. Though the shells as such are frictionless, due to the thin layer of liquid in between them, the solid surface allows friction to be incorporated by surface coatings and/or making the particle surface rough, e.g., by adsorption of small particles [36,37]. The mechanical response of these particles can be varied from soft to hard by tuning the thickness of the shell membrane [38,39]. There has been increased computational progress recently in modeling jammed granular packings of nonspherical particles [40–45], but experimental realizations are challenging. In our previous

studies, we showed that the shape of our elastic shells can be tuned from a spherical to a nonspherical bowl shape of varying bowl depth by a buckling process [32]. Moreover, by using appropriate solvent mixtures, the shells can be simultaneously index and density matched, which offers opportunities to begin from an unjammed state. In this paper we focus however on initially spherical shells already close to a jammed state (point J). Apart from understanding the physics of jamming, studying the mechanical and geometrical features of packing of shells is equally important from an application perspective as these shells find many applications, especially in industries like food, paint, and cosmetics as micro-encapsulant [46–51]. So far mechanical studies on shell-like particles or "microcapsules" have mainly been performed on a single-particle level [31,52] rather than on collections of particles that strongly interact.

In our previous article we introduced our granular models system and how it can be used to measure all the forces on particles under stress with a focus on an investigation of the microstructure and geometrical features of random packings of these shells as a function of volume fraction above the jamming point. Studies were performed in 3D real space using a confocal microscope, where the fluorescently labeled shells were dispersed in an index matched solvent to avoid scattering. From the obtained 3D image stacks, we determined the particle coordinates and radii with subpixel resolution by image processing algorithms, specially developed for these shells. In a dilute state shells underwent slight Brownian motion (self-diffusion coefficient = 0.07 μm^2/s, which translates to a time of 360 s for this particles to diffuse a distance equal to its diameter), but when the density was increased particles came in close contact and were arrested in a jammed state. Near the jamming point, the majority of particles remained spherical with little deformation at the contact points. But with increasing volume fraction, they deformed in such a way that their volume was reduced. In each contact, one of the shells buckled with a dimple at the contact region, while the other one remained spherical. This distinguishes them from emulsions, foams, and thermosensitive hydrogel particles, jammed packings of which have also been studied [11–13,15,16,53,54]. Note that the buckling of the shell is fully reversible. This we checked by releasing the stress acting on individual particles in a respective strongly compressed packing and reported in detail in Ref. [29]. It only took less than 2 min for a completely emptied or buckled shell to relax back to its uncompressed original spherical shape. We also found that this process of buckling towards one particle or the other was volume fraction dependent. At lower volume fractions it was found to be a random process but at higher volume fractions dimpling became gradually nonrandom, such that particles with a small number of contacts tend to receive more than their share of dimples; on the other hand particles having a large number of contacts tended to make a dimple on their neighbors.

This article is a followup where we utilize the stress sensing capability of individual shells by measuring the restoring forces and thereby analyzing the contact force distribution, a signature of jamming, under two kind of applied stresses: compression in a gravitational field and shear. To calculate the magnitude of the interparticle forces at each contact the quantity that we measure from the image stacks is the amount

of deformation of each particle in all directions. For elastic shells the amount of deformation can be related to the restoring force by the theory of elasticity of thin shells [9,55]. The theory predicts a linear force law at small deformations and a crossover to square root behavior at large deformations where the particles were found to form dimples. A square root variation differs from the harmonic force law that is used to describe emulsion droplets and foam bubbles [11–13,15,53], as well as from the Hertzian force law that applies to solid spheres, such as glass beads. In the present study we first focus on the measurement of the normal component of the contact forces (friction is negligible) and the force distributions in a range of volume fractions: from a marginally jammed state (close to jamming point) to a deeply jammed solid. Further, from the measured contact forces and the distances between the particle pairs we determined the global pressure and analyze how it scales with the packing density.

In the second part we describe a preliminary experiment on the behavior of shells under applied shear. Here our first results are limited to small shear strains. Although it is demonstrated that a significant shear can be applied on this system, the conditions to prevent slip at the walls were not yet optimized. We started with a jammed solid such that the shells were already deformed before a controlled shear was applied. First we looked at the effect of shear on the microstructure of jammed shells, by analyzing the projection of the radial distribution function $g(r)$ in the shear velocity-gradient plane and the changes in the number of contacts per particle for different values of strain ($\gamma < 1$; see Fig. 1). Then we studied the changes in the probability distribution of the contact forces

FIG. 1. (a) Schematic of the shear cell. The sample between the glass plates is strained by moving the top plate a distance A in the direction of the X axis that together with the Y axis forms planes parallel to the imaging planes of the microscope. The movement of the plate creates a velocity field along the X axis of the microscope and a gradient along the Z axis. The curl of the field, the vorticity, is oriented along the Y axis. (b) Confocal micrographs of jammed packing of shells before being subjected to shear in a XZ, XY, and YZ plane. Image size in XY is 1024×1024 pixels ($106.25\,\mu$m) and 352 slices ($33.26\,\mu$m) in Z.

and the anisotropy in the force network, as, for example, would be caused by force chains, in the packing that resulted from the applied shear deformation.

II. EXPERIMENTAL METHOD

A. Static shell packings

Monodisperse, several micron-sized elastic shells of tetraethoxysilane crosslinked polydimethylsiloxane used were prepared by an emulsion templating technique. The template polydimethylsiloxane (PDMS) oil droplets were obtained by using a Turrax homogenizer for the efficient mixing of reactants followed by droplet growth without external agitation [29,30]. The system used for this study is same as that of Ref. [29] and contained particles of radius $R_t = 2.88 \pm 0.03\,\mu$m with polydispersity $\sim 3\%$ and a shell thickness $d = 56 \pm 2\,$nm. This corresponds to a shell thickness to particle radius, $d/R_t = 0.02$. The aforementioned radius denote the value obtained by static light scattering (SLS) measurement and the shell thickness was obtained from atomic force microscopy (AFM). To enable 3D confocal microscopy, the rhodamine B-isothiocyanate (RITC, Sigma-Aldrich) labeled shells, after removing the PDMS droplet template by solvent exchange, were dispersed in an index-matched solvent of dimethyl sulfoxide (DMSO, 52.6% v/v) and ethanol (47.4% v/v) of refractive index $n_D^{20} = 1.42$.

A detailed description of the experimental procedure to create packings of shells of different volume fractions and of 3D image analysis routines to find the coordinates and radii of particles can be found in our recent article on jammed shells [29]. Briefly, random packings of compressed shells were prepared in capillaries of typical dimensions $0.1 \times 1 \times 50\,$mm or $0.1 \times 2 \times 50\,$mm (depth $\times$ width $\times$ length, Vitro-Com) with a wall thickness $0.1\,$mm by centrifugation, with the length of the capillary along the direction of gravity. Without disturbing the capillary, volumes of size $99.94 \times 99.94 \times 86.43\,\mu$m^3 ($1024 \times 1024 \times 790$ voxels with a voxel size of $0.0976 \times 0.0976 \times 0.1094\,\mu$m^3) were imaged at different heights in the sediment using a Nikon C1 confocal microscope with a $63\times$ NA 1.4 oil immersion objective (Nikon) in fluorescence mode. Average radii and polydispersity obtained from image analysis [29] were $2.952 \pm 0.002\,\mu$m and 6% respectively. The radii of the particles obtained from image analysis is close to the value that was obtained from SLS, which is more accurate, but polydispersity is slightly higher resulting from the inaccuracies in image analysis. The volume fraction of each imaged volume was obtained from the image analysis and can be found in Table 1 in Ref. [29] and in Table S1 [56].

B. Sheared shell packings

The sample for the shear experiments consisted of shells of radius $R_t = 2.16 \pm 0.03\,\mu$m with polydispersity 3%, measured by SLS and a shell thickness $d = 30\,$nm ($d/R_t = 0.013$), measured by AFM. The average radius of the particles measured from the image analysis was $R_t = 2.20\,\mu$m with polydispersity 5%. This size is only 40 nm larger than the size obtained from light scattering measurements. To study the effect of shear on our shell packings, we prepared a
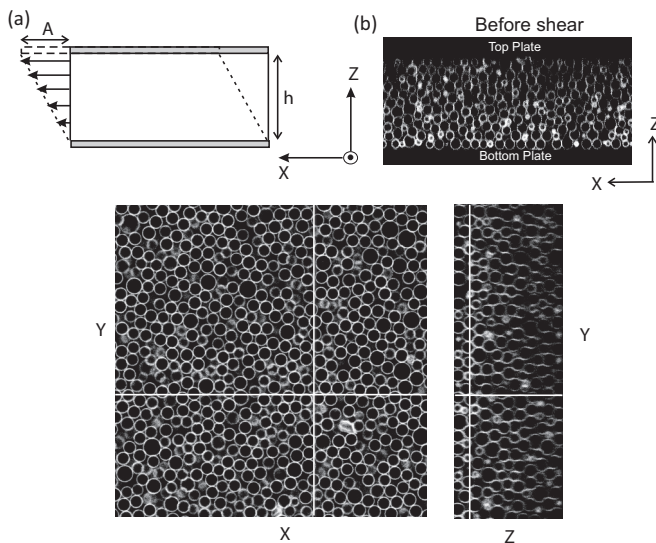
concentrated suspension of shells again by centrifugation, but this time in an Eppendorf tube. After centrifugation, the surplus solvent was removed, and the sample (in the form of a paste) was carefully scooped out and placed between two parallel microscope glass slides that had been attached to the bottom and top cassettes of a parallel plate shear cell. The shear cell was mounted on top of an inverted confocal scanning laser microscope (Leica TCS-SP2) for real-space imaging. Details of the design and layout of the shear cell are described in Ref. [57]. In brief, on the bottom cassette a glass coverslip (Menzel Gläzer, no. 1.5, thickness 0.15–0.17 mm) of 24×50 mm and on the top cassette a microscopy glass slide (Menzel Gläzer, thickness 1–1.5 mm) cut to 9×29 mm were attached, following the method described in Ref. [57]. In order to apply a shear strain to the sample, these cassettes were placed in translational stages that were displaced by piezostepper motors. Before loading the sample the glass plates were carefully aligned parallel to each other with adjustment screws. This is important in order to create a uniform and parallel shear flow. The alignment was determined with confocal microscopy in reflection mode using an Argon 488 nm laser and an air objective (20×0.7 NA, Leica). After alignment the objective was changed for an oil immersion objective (63×1.4 NA, Leica) that was used for imaging, and the gap width was set ($h \approx 46 \mu$m). The vapor barrier of the bottom cassette was filled with water, and a few droplets of solvent were dropped into the vapor gully to minimize evaporation of the sample. After that, the sample was placed on the glass slide of the bottom cassette. Finally, the top cassette (with the metal vapor lock attached to it) was carefully and slowly lowered on top of the sample. We observed that the sample spread uniformly in several seconds, and the concentration remained homogeneous between the plates as we overfill the cell. Figure 1(a) shows a schematic representation of the shear cell. The top plate (gray) was then translated from its initial position by a distance A with a velocity v_t that can be set during the experiment. The bottom plate was kept stationary as the speeds in our experiments was very small, but normally this plate can be driven as well. The movement of the plate creates a velocity field along the X axis of the microscope and a gradient along the Z axis. The curl of the field, the vorticity, is oriented along the Y axis.

Before shearing the sample was left to equilibrate for 15–20 min. Then a shear was applied to the system by moving the top plate to a final amplitude of $A = 20 \mu$m in steps of 5μm with a slow, constant speed of $v_t = 10$ nm/s, to limit the risk of wall slip. This corresponds to a shear rate of $\dot{\gamma} \equiv v_t/h =$ 0.217×10^{-3} s^{-1} and a total applied shear strain $\gamma \equiv A/h =$ 0.434 in steps of 0.11. During each shear step a time series of XZ scans covering the whole gap from plate to plate was taken. Before shearing the sample a XYZ stack was acquired as a reference. Then the top plate was moved 20μm with a speed 10 nm/s in successive steps. After each shear step a new XYZ stack of the sample volume was taken. The size of the image volume is $106.25 \times 106.25 \times 33.26 \mu$m^3 ($1024 \times 1024 \times 352$ voxels with a voxel size of $0.1037 \times 0.1037 \times 0.0945 \mu$m^3). The voxel size in Z was corrected for index mismatch with a scaling factor 0.91 [58,59]. The acquisition time for each image stack was approximately 25 min, during which no particle motion or restructuring was observed as confirmed from XZ time series data. The 2D confocal images of the sample in a XZ, XY, and YZ plane before are shown in Fig. 1(b). The shells are clearly jammed and deformed between the parallel plates.

The coordinates of the particles were obtained through the image analysis procedure as described in Ref. [29] for static packings. Table I gives an overview of the sample before shear and at different values of the shear strains. We measured the actual strain in the sample by measuring the change in position of the shells next to the top plate from their initial position after each shear step. By looking at the displacement of shells at other positions we found that the shear was uniform throughout the gap. The measured strain was found to stay behind the applied strain, especially for the largest strain. For shear 4 the measured strain was just half the total applied strain, and thereafter the shells no longer followed the plate movement at all due to complete slip at the moving upper plate. Note that we tried a few methods to avoid wall slip, for example, by introducing roughness on to the plate by abrasion and by adsorbing 5μm polymethylmethacrylate (PMMA) particles to the plate. Both methods failed to prevent the wall slip; on the contrary, the rough plates were found to enhance slipping of the shells near the plate. Untreated glass plates were found to work better for the shear experiment. Moreover, we also noticed that repeated use of the same glass plates for shearing of the shells also enhanced wall slip. We hypothesize that this is caused by the adsorption of polyvinylpyrrolidone (PVP) that sterically stabilizes the shells to the glass plate, modifying the plate surface and thereby preventing the shells from sticking to the plate. This hypothesis needs to be investigated further in order to obtain optimized walls with (much) less slip. For the experiments reported in this paper, where a slow small strain was applied sequentially, the plates were not new, and they were used beforehand a couple of times and this might have

TABLE I. Details of the image stacks obtained from image analysis algorithms from the sample before undergoing shear and after the sample had been strained by a total strain 0.434 in four steps.

Image stack	Applied strain	Measured strain	No. of particles	Image volume (μm^3)	No. of contacts	Average contact number, $\langle Z \rangle$	ϕ	$\langle F \rangle$ (μN)	$\sigma_F/\langle F \rangle$ (%)
Before shear	0	0	5321	290 444	21 504	8.79	0.835	0.0147	30.13
Shear1	0.108	0.093	4697	264 465	19 237	9.01	0.784	0.0158	33.75
Shear2	0.217	0.169	4613	264 470	18 733	8.99	0.758	0.0159	36.47
Shear3	0.326	0.204	4592	264 675	18 502	8.93	0.755	0.0160	36.47
Shear4	0.434	0.216	4775	264 631	19 416	8.99	0.778	0.0154	37.01

led to increased slipping near the shearing surface towards the end of the experiments.

The number of particles listed in the table was obtained from an image volume that avoided one layer of particles close to both the glass plates. From the Z coordinates obtained from the analysis we found a 9% reduction in the height h for the sample just after the first shear step, which then later remained unchanged. This reduction in the gap width between the plates resulted probably from relaxation of the bottom plate, which may have been slightly bent by the weight of the top cassette when it was put on and was transferred through the suspension of jammed shells.

The volume fractions of these packings were calculated by summing the volumes of the spheres and subtracting their overlap volumes in the image volume as described in Ref. [29] and are listed in Table I. The image volumes correspond to the product of the length in X and Y directions that are reduced by an amount R_t (average radius obtained from image analysis) from both sides to compensate for the particles that are missing near the edge (not identified during image analysis) and in the Z direction to exclude one layer of particles close to both the glass plates. For particles straddling the edges of the reduced volume it is somewhat arbitrary how much of their volume should be included in the volume fraction measurement. This produced an uncertainty of about 0.005 in the determination of the volume fraction. The difference in the image volume and in the number of particles between different shear experiments mostly resulted from the reduction of the gap width due to the relaxation of the bottom plate combined with slight discrepancies in the cutoff values chosen along the gap width to remove particles close to the wall. We determined the number of contacts for each shell from the coordinates of their centers and radii [29]. A pair of particles is considered a contact pair if the distance between their centers is less than or equal to the sum of their radii. The chances of missing a contact in our system are determined by the resolution in finding the radii and particle position (which is less than one pixel, about 80 nm).

C. Contact forces between buckled shells

In a jammed system of spherical elastic shells, the shells deform at regions where they are in contact with each other. Figures 2(a) and 2(b) shows confocal images of jammed shells ($d/R_t = 0.02$) at volume fractions $\varphi = 0.663$ and $\varphi = 0.908$. At low φ, near the jamming point, the deformation of the shells should not be prominent; obviously in the image [Fig. 2(a)] there is no noticeable change in the shape of the contact region. However, for $\varphi = 0.908$ the shells were clearly deformed, and the contact regions were buckled with shells making or receiving an indentation from their neighbors. For each pair of contacting particles i and j the interparticle contact force can be determined by measuring the depth of the indentation, i.e., the deflection of the shell at the contact point δ_{ij}. For a pair of shells of radii R_i and R_j, the deflection δ_{ij} [Fig. 2(c)] is

$$\delta_{ij} = (R_i + R_j) - \ell_{ij}, \qquad (1)$$

where ℓ_{ij} is the distance between their centers.

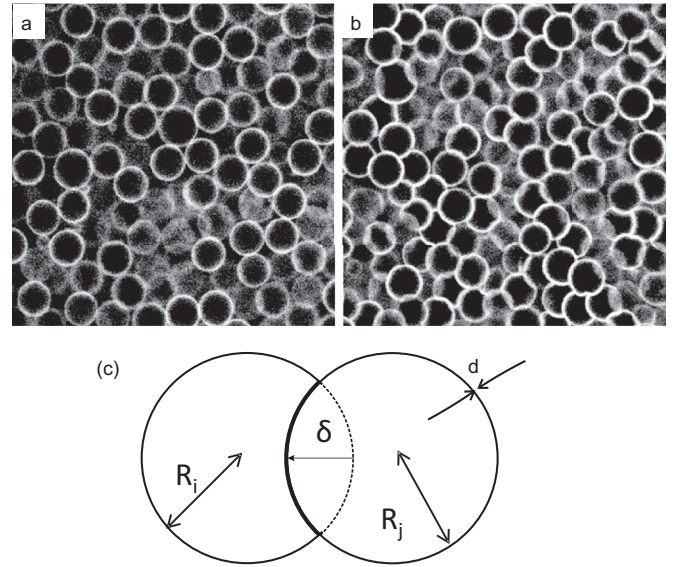The deflection δ_{ij} can be related to the force acting at the contact region by a force law derived from the theory of

FIG. 2. Confocal images of shells at volume fractions (a) $\varphi = 0.663$ and (b) $\varphi = 0.908$. Image size is 550×550 pixels. (c) Schematic of a contact pair where, particle j of radius R_j makes an indentation in particle i of radius R_i. The depth of the indentation is δ_{ij}, and d is the thickness of the shell.

elasticity of shells [9,55]. Under a small localized load a thin elastic shell is predicted to respond linearly to the indentation magnitude up to about the shell thickness (d) [60,61]:

$$F_{ij} = k \frac{\delta_{ij}}{R_{ij}}, \qquad (2)$$

where $k = 2Ed^2/\sqrt{3(1 - \nu^2)}$ and $R_{ij} = (R_i + R_j)/2$ is the average radius of the particles i and j measured from the microscope data. For these elastic shells the value of the Young's modulus (E) and the Poisson ratio (ν) are 200 MPa and 0.3, respectively, as reported in Ref. [31].

If the deflection is beyond the shell thickness, the shell undergoes *mirror buckling* [Figs. 2(b) and 2(c)]. This leads to an inversion of curvature of the shell, i.e., the formation of a dimple at the contact region. The major part of the elastic energy is then concentrated in the *bending strip* near the edge of the dimple, whose radius grows with the indentation. The magnitude of the applied force is then proportional to the square root of the indentation [55]:

$$F_{ij} = c \sqrt{\frac{\delta_{ij}}{R_{ij}}}, \qquad (3)$$

where $c = 0.534Ed^{5/2}\pi/(1 - \nu^2)\sqrt{R}$. To obtain more accurate forces we use the ratio δ_{ij}/R_{ij} obtained from the microscopy data, and R from the (more accurate) light-scattering measurement.

The above solution for the deformation of a shell was obtained through a geometric approach and following the assumption that the applied load is conservative, i.e., the work it performs under deformation of the shell depends only on the final shape and not on the path it followed [9,55]. Equation (3) was derived for a point load, but the final shape is a spherical dimple, which is the same as for a pair of contacting

equal-sized spheres. If the shape is the same as for a point contact, the elastic energy must also be the same (if it is conservative). Then the restoring force between the spheres is the same as the force applied by a point load, as it is the derivative of the elastic energy. We therefore expect Eq. (3) to hold in our experiment, where two spherical shells of almost equal radius and elasticity are in contact and only one of the shells is dimpled at the contact point as shown in Fig. 2(c).

For large deformations of a spherical shell, it is also important to take in to account the permeability of shell membrane or volume conservation [9,62]. The volume of an impermeable shell with an incompressible fluid is constrained. This results in an additional restoring force that arises due to the stretching of the membrane to keep its volume conserved while the shell is deformed. Clearly in the packing of our elastic shells filled with index-matched solvent, during the time of the experiment, the shells were fully permeable to the solvent on the time scale of the deformations, which resulted in the formation of dimples. However, if instead of solvent-filled shells, shells filled with polydimethysiloxane (PDMS) oil dispersed in an index-matching water and glycerol mixture were compressed, the content could not leave the shells to mix with the solvent, and the shells had to deform in such a way as to conserve their inner volume. Such a case is shown in the confocal image [Fig. 3(a)], where shells filled with PDMS oil were confined between two glass plates. Here the deformation was completely different as compared to solvent permeable shells. The shells became flattened at the contact regions and are bulged at noncontact areas. The final shapes of these shells resemble the deformation of oil droplets in compressed emulsions [12,13], where instead of membrane elasticity the deformation energy is dominated by the interfacial tension. We would like to note here that, from experiments on the release of oil from inside the shell by micelles, it had become evident that the shells were permeable to the inner oil [32]. These results show the possibility to modulate the interaction potential and even particle volume in one single system that can lead to different mechanical properties, which is rare. However, in the present experiments there were no micelles to solubilize
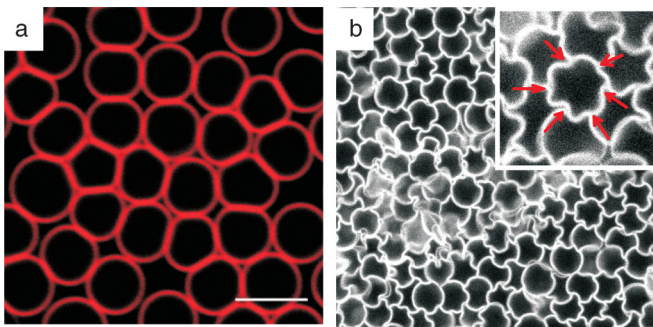

FIG. 3. Confocal images of alternately deformed shells: (a) Filled with PDMS oil, dispersed in an index matched water and glycerol mixture, confined between two glass plates. The red contours represents the shell walls. The deformation of these shells was completely different from those in the force measurements. (b) Filled with an index matched solvent at extreme compression $\varphi \approx 1$. Inset is a zoomed in picture of a shell with wrinkles. The arrows point to the dimples created on this shell by its neighbors. The scale bar in both pictures represents 5 μm.

that oil, and therefore the shells acted like an impermeable membrane for the oil inside.

In principle, to determine all the contact force magnitudes we should use the linear force law [Eq. (2)] for small deformations and the nonlinear force law for large deformations [Eq. (3)] where one particle buckles with a dimple. Unfortunately, an analytical force law valid for arbitrary deformation does not appear to be available. Theoretically, the cutoff value of the overlap depth δ_{ij} where the linear and the square root force laws intersect is at about twice the shell thickness ($\approx 2d$). In the packing at $\varphi = 0.663$, about 40% of the contacts have an overlap depth $\delta_{ij} < 2d$, which is rather high, but this value decreased rapidly with increasing volume fraction [a plot of fraction of contacts with $\delta_{ij} < 2d$ as a function of volume fraction is shown in Fig. S1(A) [56]]. Although the differences in the forces found with Eq. (2) or Eq. (3) are not large, use of Eq. (3) irrespective of deformation would lead to a severe underestimation of the number of small contact forces in a packing [Fig. S1(B) [56]]. On the other hand, attempting to use the correct force law in each of the two regimes led to an undesired discontinuity in the force distributions [Fig. S1(B) [56]]. Note that this discontinuity in force distribution is purely an artifact and not a physical event, as indentation always grows continuously with the force [31,63]. To overcome this problem we derived an empirical formula that we call stitching force law as it interpolates smoothly between the linear and nonlinear behavior:

$$F = \frac{c^2}{2k}\left[\sqrt{1 + \frac{4k^2\left(\frac{\delta_{ij}}{R_{ij}}\right)}{c^2}} - 1 + 0.92\frac{\left(\frac{\delta_{ij}}{R_{ij}}\right)^2}{\left(\frac{\delta_{ij}}{R_{ij}}\right)^2 + \frac{c^4}{k^4}}\right]. \quad (4)$$

The factor 0.92 was chosen to obtain the best fit to the known limits at small and large deformations. A detailed derivation of this stitching force law is described in the supporting information. It was compared with atomic force microscopy measurements on similar shells from the literature [31], and good agreement was found [Fig. S1(D) [56]].

In this work interactions that result from elastic deformation dominate the usual colloidal interactions. Many body interactions will arise when two or more dimples from different particles come close to each other. So at high volume fractions these may become important. Then we also start seeing the irregular deformations. The densest packing that we analyzed in our experiments on compressed elastic shells was of volume fraction $\varphi \approx 0.9$ [29]. Further increase of the number of particles in a finite volume did not appreciably increase the volume fraction, which is a likely indication that the volume squeezed out of the system came mainly from a reduction of shell volumes rather than a reduction of interstitial spaces. However, for completeness we mention that we have seen packings where the shells occupy nearly all the interstitial spaces leading to a volume fraction of almost unity by deforming as shown in Fig. 3(b). This high packing fraction of shells was partly obtained by slow solvent evaporation from an already jammed system. For this case the shells started to *wrinkle* and formed highly interlocked *cogwheel-like* structures. By wrinkling we mean the formation of more than one dimple at the contact region between a contact pair. The inset figure is a zoomed-in image of a
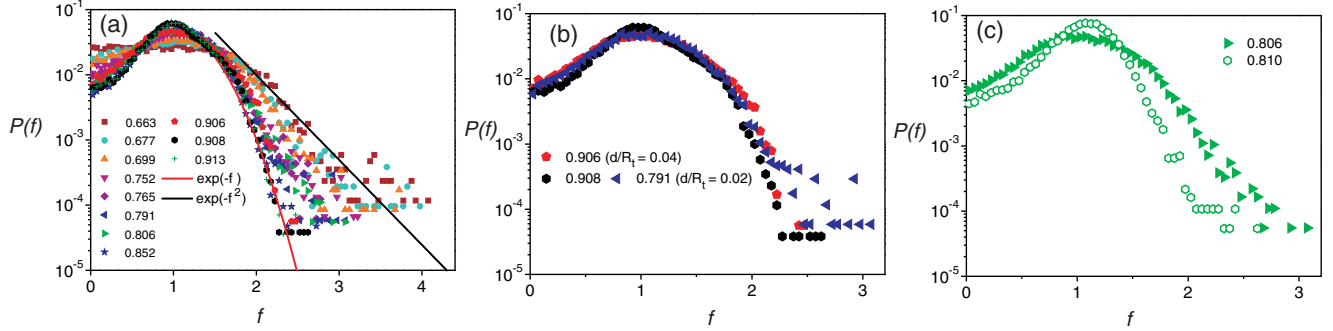
FIG. 4. Probability distributions of the contact forces normalized by the average contact force, $P(f)$ ($f = F/\langle F \rangle$) for (a) a range of experimental volume fractions, φ, above the jamming point, (b) the sample with a thicker shell compared with a thin shell system at similar φ, and with a thin shell system with a similar distribution, and (c) the sample with higher order compared with a disordered sample with similar φ. Solid lines in (a) are exponential and Gaussian fits for the lowest and highest volume fractions. Note that in the tails, the distributions have data points forming horizontal lines. This is due to the smaller value of the number of counts in the histogram.

shell with six neighbors in a 2D plane. The arrows point to dimples formed on this shell by its neighbors. These dimples were most likely created by the forces exerted by the sharp cusps of neighbor particles. The new dimples were formed on the shells, which initially remained spherical at the contact region. They appear to have formed when one of the shells invaded the remaining interstitial space. In this case the square root relation between the contact force and the depth of the indentation between a pair of particles is not expected to be valid anymore. Moreover, the image analysis routines used become unreliable for these shapes, making it difficult to analyze these structures. However, the extreme interlocking and mechanical entanglement of particle surfaces can lead to interesting bulk mechanical properties, which could be explored in the future.

III. RESULTS AND DISCUSSION

A. Static shell packings

Here we focus on the probability and spatial distribution of the contact forces and subsequently scaling of pressure as a function of volume fraction in static packings of our shells compacted with a gravitational field.

1. Probability distribution of the contact forces as a function of volume fraction

We calculated the magnitudes of the contact forces for all particle pairs with overlap depth $\delta_{ij} > 0$ using the force law Eq. (4). The error in force magnitude in our experiment depends on the error in the overlap depth, which in turn is limited by the resolution in finding the coordinates of the shells. The coordinates of the shells were obtained with an error less than one pixel (0.080 μm in X_c and Y_c and 0.073 μm in Z_c) [29]. This leads to an error of approximately $\pm 0.026\,\mu$N in the contact force magnitudes (forces less than 0.026 μN are clearly unreliable). This is close to the value of the average force measured in the packing at the lowest volume fraction (for $\varphi = 0.663$, $\langle F \rangle = 0.031\,\mu$N; see Table S1 [56]) but below that of more compressed packings. However, the total force on each particle is zero within the experimental error. With an error of 0.026 μN in each contact force in a random direction

we obtain a root mean square error of 0.06 to 0.08 μN for $N = 6$ to 12 forces on a particle. The measured average of total force on each particle is found to be 0.06 to 0.08 μN for packings with 6 to 12 contacts, which is the same as the root mean square error. Therefore the nonzero value of total force is completely a contribution from the position error.

Figure 4(a) shows the probability distributions of the contact force magnitudes normalized by the average force at different volume fractions away from the jamming point. For the lowest volume fraction, the distribution is uniform near small forces but decays above the mean, at larger forces. This clearly reflects the heterogeneity in the contact force magnitudes in these packings. As the volume fraction increases, the distribution was found to peak around the mean, the maximum becoming more pronounced with increasing packing fraction. Moreover, the tail became steeper. The tail can approximately be fitted with an exponential and a Gaussian for the lowest and highest volume fractions, respectively, as shown in Fig. 4(a). In other words, the tail of the distributions was found to decay roughly exponentially for the lowest volume fractions and to crossover to a Gaussian at the highest volume fractions, qualitatively similar to the results reported in simulations and experiments on 2D and 3D soft deformable granular systems [11,12,14,21,22]. The evidence for transition of $P(f)$ from a pure exponential for small deformations to a Gaussian centered at $f = 1$ when particle deformation is increased at higher compression was first reported in simulations and experiments performed by Makse *et al.* [21]. The observed crossover is associated with a loss of localization of force chains that span the system at high applied stress. Near the critical density, or point J, the grains are weakly deformed but still well connected, and hence a broad force distribution is found. As the system is compressed further, new contacts are created and the density of force chains increases. This in turn gives rise to a more homogeneous spatial distribution of forces.

Note that the packing at $\varphi = 0.906$ consisted of slightly stiffer shells (shell thickness to radius ratio, $d/R_t = 0.04$) in contrast to all the other volume fractions ($d/R_t = 0.02$). As a result, for the same amount of deformation, the average value of the contact forces in $\varphi = 0.906$ was higher ($\langle F \rangle = 0.27\,\mu$N) compared to the soft shell packing corresponding to

a volume fraction $\varphi = 0.908$ ($\langle F \rangle = 0.074\,\mu$N). Moreover, the shape of $P(f)$ was also slightly different for the stiffer shells: in particular the tail is less steep and the peak around the mean is broader [Fig. 4(b)]. A similar trend in the force distribution was also observed experimentally in a 3D compressible granular packing with an increase in hardness of individual grains [6]. In our case, the shape of $P(f)$ in the stiff shell packing actually coincides more closely with the packing at $\varphi = 0.791$ ($\langle F \rangle = 0.054\,\mu$N) containing less stiff shells [Fig. 4(b)]. Thus, clearly, as expected, the stiffness of the constituent particle has an effect on the distribution of forces in jammed materials.

The distribution shown by the open symbol in Fig. 4(a) represents the packing of $\varphi = 0.810$, which showed a split second peak in the radial distribution function, $g(r)$, and that did not fall in the trend of other packings as shown in Ref. [29]. This packing also exhibited a similar discrepancy in the force distribution as well. The $P(f)$ of this packing showed a slightly higher peak near the mean force and a steeper tail compared to all other volume fractions, including the disordered sample with similar φ, shown in Fig. 4(c). A similar observation has been previously reported by Blair *et al.* [5] for a crystalline packing in a 2D experimental study on the effect of particle order on the distribution of the contact forces. Thus, our results on the force distribution (along with its radial distribution function [29]) are consistent with a slight order in our packing of shells at $\varphi = 0.810$ and $\varphi = 0.835$ (not shown), which was, however, neither observed visually in the confocal images nor in a local bond order analysis [29].

2. Force networks

Having found the coordinates of the particles and their respective interparticle forces, our experimental data allow us to examine the spatial distribution of the contact forces in the different volume fractions of our compressed elastic shells. The forces are represented by tubes connecting the centers of the contact pairs. Figures 5(a) and 5(b) shows the force networks in shell packings at low and high volume fractions, $\varphi = 0.699$ and $\varphi = 0.908$ (magnified view of the force networks in these sample volumes are shown in Fig. S2 [56]). Only forces above 1.5 times the average force are shown in the figure. The thickness of the tube and its color are proportional to the force magnitude. The box dimensions given in Fig. 5 correlate to the length, width, and depth in the capillary tube in which the packings of shells were prepared. In $\varphi = 0.699$ the force network is nearly isotropic, in contrast to the high volume fraction packing $\varphi = 0.908$, where the direction of the force segments tended to align along the X direction, which is the direction of gravity. This is also the direction in which the shells were subjected to an uniaxial compression in the capillary (as described in the experimental method). Not only for the above packings, but also for other volume fractions, we saw a clear difference in the directionality of the average stress; lower φ being more isotropic than higher φ. This is quantitatively shown in Figs. 5(c) and 5(d), in a plot of the spatial orientation of the contacts carrying larger forces at different volume fractions. The observed isotropy at low volume fractions is likely due to the uniform confinement of
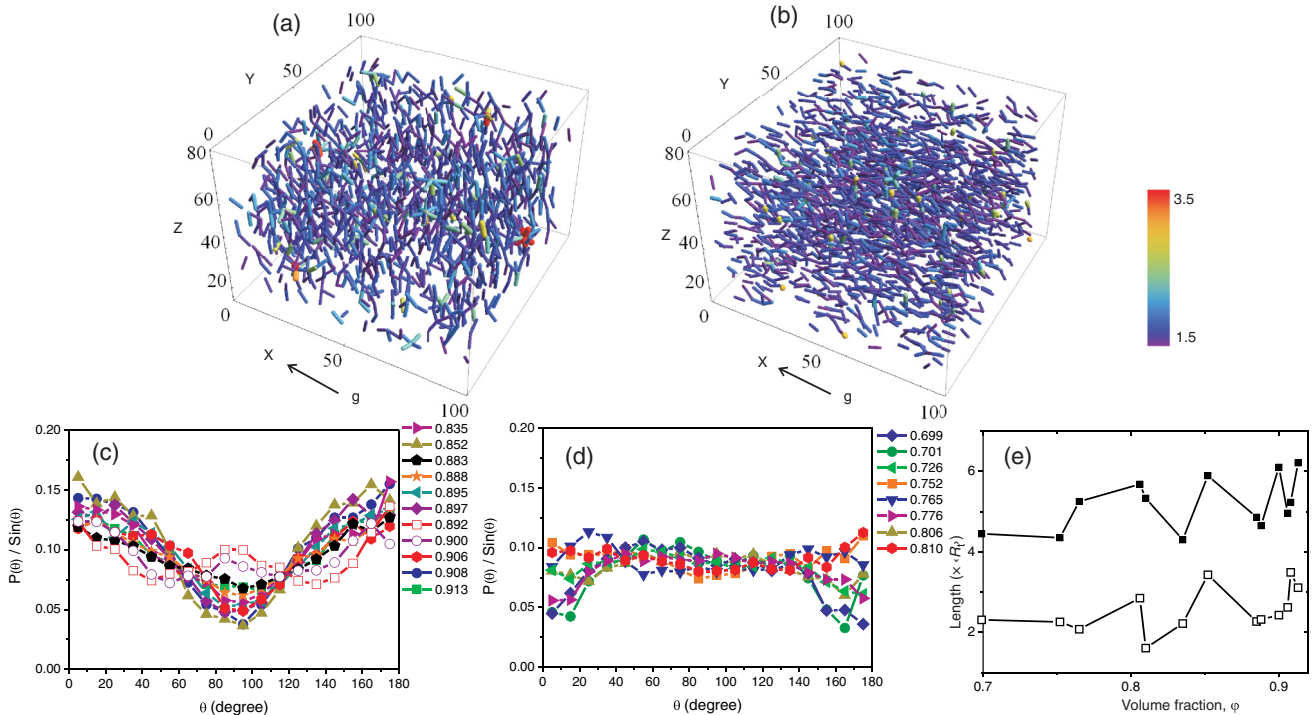

FIG. 5. Force networks in compressed shells in the lowest and highest packing fractions, (a) $\varphi = 0.699$ and (b) $\varphi = 0.908$ for forces greater than 1.5 times the average value. Forces, in units of the average force $\langle F \rangle$ are represented by tubes connecting the centers of contact pairs where the thickness and color of the tube is proportional to the magnitude of the normal force. Red indicates a force 3.5 times larger than the average force. The X axis is the direction of gravity. (c) and (d) Probability distribution of angles with respect to gravity for contacts carrying above average force in compressed packings of shells at high and low φ. (e) Graphical representation of change in average chain length (closed square) and persistence length (open square) of force chains obtained from shell packings under compression.

the shells by the capillary walls along the Y and Z directions and from the weight of the shells on top of the sediment in the X direction. This weight of course is decreasing with distance to the bottom of sediment (see figure in Ref. [29]) leading to the anisotropic stress distributions observed at higher φ.

In both packings, in addition to many isolated segments there are also short force chains that are tenuous and not well defined. In addition to 3D visualization of the force networks, a more quantitative search for the existence of force chains was also performed (supporting information). Force chains, i.e., contacts carrying larger forces, were described in many experimental systems with anisotropic stresses, for example, in a 2D granular packing of photoelastic disks under shear [8], bidisperse emulsion droplets in a quasi-2D experiment [15], and polydisperse 3D piles of frictionless liquid droplets under uniaxial compression [14]. However, force chains were not seen in the 3D emulsion system studied by Brujic *et al.*, where the droplets were compressed by centrifugation [12,13]. Instead, in their admittedly small sample volume, the forces appeared to be uniformly distributed in space, and the average stress was found to be independent of direction, indicating isotropy. Our analysis of force chains was based on the definition described in the article by Desmond *et al.* on a 2D bidisperse system of emulsion droplets [15]. In this definition, a force segment between two shells in contact belongs to a chain if it is one of the two largest forces on both shells. This does not allow branching of chains and so favors the identification of chains. In our shell packings, the average length and persistence length (Table S2 [56]), a measure of the average length beyond which the chain has forgotten its original direction, were found to be 6.21 $\langle 2R_t \rangle$ and 3.11$\langle 2R_t \rangle$ ($R_t = 2.88 \pm 0.03\,\mu$m), respectively, at the highest volume fraction and 4.45 $\langle 2R_t \rangle$ and 2.31$\langle 2R_t \rangle$ at the lowest volume fraction. These numbers are rather small compared to the sample volume ($99.94 \times 99.94 \times 66\,\mu$m^3), which indeed matches the visual observation of Figs. 5(a) and 5(b). Figure 5(e) shows the variation of average chain length (closed square) and persistence length (open square) of force chains obtained from these compressed packings. The slightly higher value of the force chain length in the shell packing at high volume fraction most likely is a result of the anisotropy in the contact network [Figs. 5(c) and 5(d)].

3. Pressure

From the measured contact forces between particle pairs we calculated the pressure at each packing density, above the jamming threshold. The global pressure is determined from $P = \Sigma_i \Sigma_{j>i} F_{ij}\ell_{ij}/V$ [15,33], where V is the total 3D image volume, ℓ_{ij} is the distance between the centers of the contact pairs. The calculated value of P varied from 2.57 kPa to 18.93 kPa for the experimental range of φ [Fig. 6(a)]. The nonzero value of the pressure at the lowest value of φ resulted from the error in the measurement of the overlap depth and the radii of the shells. Since the contact forces must be positive, this leads to a finite pressure where it should be almost zero. Therefore, we subtracted from the measured pressures an amount $P_c = 3.98$ kPa, which was the pressure close to $\varphi_c = 0.683$ (pressure at $\varphi = 0.677$) obtained from a power law fit of Z.

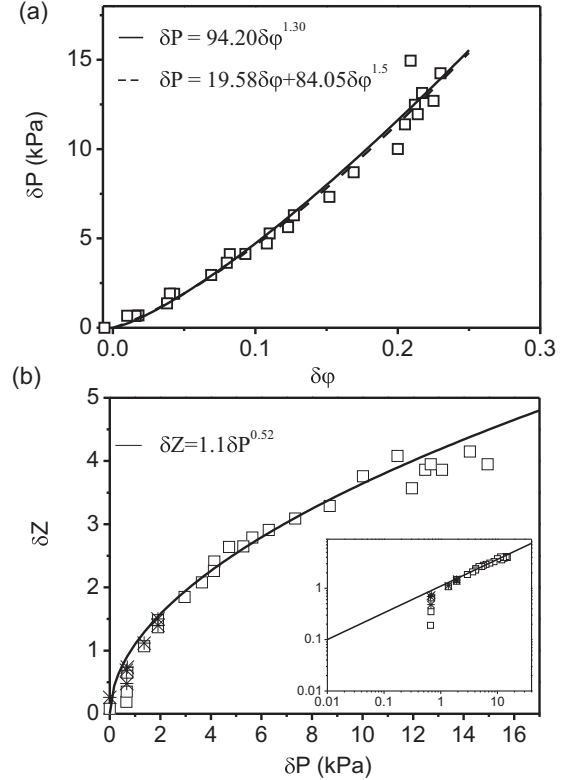FIG. 6. (a) Scaling of excess pressure δP with volume fraction $\delta\varphi$ above the jamming point ($\varphi_c = 0.683$). The lines are fits to the experimental data. (b) The variation of excess contact numbers δZ with pressure that follows a nonlinear power law of exponent 0.52 (solid line). The data points marked by asterisks are the Z values avoiding the rattlers. The inset graph shows a double logarithmic plot.

The predicted scaling of the pressure as a function of volume fraction from numerical simulations [20] is $P - P_c = P_0(\varphi - \varphi_c)^{\alpha-1}$, with the exponent $(\alpha - 1)$ the same as for the force law. Here α is the exponent of the interaction potential, which is 2 for the harmonic interaction and 2.5 for a Hertzian. In our system of shells, the force is linearly related to the deformation only near contact and crosses over to a square root variation at higher deformations. Even close to the jamming point only 40% of the contacts fall in the linear regime, and this number drops with increasing φ. Moreover, in this regime the magnitude of the force calculated from the linear and nonlinear force laws is small. Therefore, we expect the value of exponent to be in the range $0.5 \leqslant (\alpha - 1) < 1$. However, this does not agree with the experimental data in Fig. 6(a). If anything, the experimental value of $(\alpha - 1)$ is found to be slightly larger than 1, a value of 1.30 is obtained from the fit. Furthermore, the scaling of the excess contact numbers δZ with pressure δP was also found to deviate from the predicted linear power law, which is obtained by considering the effect of applied stress on density of vibrational modes $D(w)$ described in Ref. [64], shown in Fig. 6(b). Note that the fit in Fig. 6(b) corresponds to $\delta Z = 1.10\delta P^{0.52}$, where the fit parameters are equivalent to the prefactor and exponent obtained by solving the power law scaling: $\delta Z = 11.39\delta\varphi^{0.681}$

shown in Ref. [29] and $\delta P = 94.20\delta\varphi^{1.30}$. Hence, the three scaling laws are interdependent.

A similar deviation of pressure scaling from the predicted power law was also observed for emulsion droplets, both in two and three dimensions [15,65]. However, in 2D photoelastic disks the reported value of $(\alpha - 1) = 1.1$ was in good agreement with simulation results, but the range in the density was rather narrow, only 1% [10]. The reason for this deviation in a compressed emulsion system [65] was explained based on the difference in the response of random elastic networks and random packings of particles to compression, as is observed numerically [66]. In random networks all the elastic moduli vanish linearly with the excess contact G (shear modulus) $\sim B$ (bulk modulus) $\sim\delta Z$; however in packing-derived networks of harmonic particles the bulk modulus remains constant down to the jamming transition, where it vanishes discontinuously. The finite value of the bulk modulus at $\delta Z = 0$ is purely geometric with contacts tending to move towards each other more prominently than to slide past each other [66]. Based on this numerical observation, that is, $B \equiv \varphi\partial P/\partial\varphi \approx C_1 + C_2\delta Z$, where C_1 and C_2 are constants, in Ref. [65] a new scaling was proposed that results in two leading order terms in $\delta\varphi$: $\delta P = (P - P_c) = P_1\delta\varphi + P_2\delta\varphi^{1.5}$. Our data can be well fitted with this power law for the full range of φ shown in Fig. 6(a) (dash line), where $P_1 = 19.58$ kPa and $P_2 = 84.05$ kPa are prefactors obtained from the fit.

B. Sheared shell packings

1. Microstructure

Here we discuss our experimental results on the effect of shear on the structure and force distributions in our jammed systems of elastic shells. The shear-induced structure of the system was analyzed by calculating the distribution functions $g(X,Z)$, $g(X,Y)$, and $g(Y,Z)$. Because of the anisotropy introduced by the shear, we made 2D cuts of a finite thickness along different planes to illustrate how the $g(r)$ is changing in 3D in the different planes. More specifically, $g(X,Z)$ is calculated by considering all pair separations in which the magnitude of the Y component of the separation satisfies $|Y| < R_t$.

Figure 7 shows $g(X,Z)$, $g(Y,Z)$ and $g(X,Y)$ for the sample before and after applying shear, for two measured consecutive strains $\gamma = 0.093$ (shear 1) and $\gamma = 0.169$ (shear 2). The three bright rings with decaying probability (indicated by color) in the plots represent the first, second, and third shell of neighbor particles. The configuration of the sample before shear, $\gamma = 0$, already shows a slight anisotropy, visible as sixfold maxima in the first-order ring, especially in the X (velocity) direction. This is probably due to less well controlled shear that occurred by the flow when the top cassette was lowered on top of the sample. The amount of change in order that this flow may have introduced appears modest as can be observed from the images in Fig. 1 and also as was confirmed by a local bond order analysis (not shown). In addition, this flow caused an uniaxial compression, which is the cause of the observed flattening of the bright rings along the Z axis. When the sample was then sheared the configuration became more asymmetric around the center where the bright rings got closer to the center as the shells were squeezed along the compression axis and stretched out along the extension
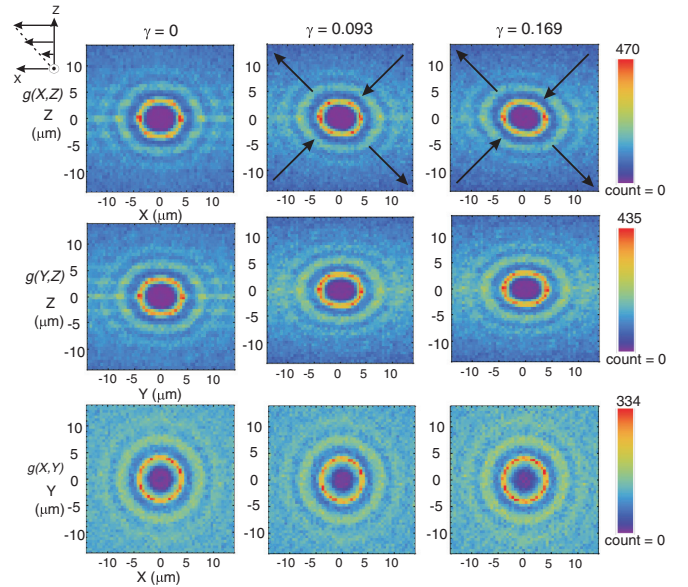

FIG. 7. Probability of interparticle distances in different planes XZ (velocity-gradient), YZ (vorticity-gradient), and XY (velocity-vorticity) for the shells before subjecting to shear and after the sample was sheared by an amount $\gamma = 0.093$ and $\gamma = 0.169$. Bin size in X, Y, and Z are $0.498\,\mu$m, $0.498\,\mu$m, and $0.504\,\mu$m, respectively. Shear-induced extension and compression are illustrated by the arrows.

axis. In the velocity-vorticity (XY) plane the configuration was symmetric and remained unaffected by this intentional shear. For $\gamma = 0.204$ and $\gamma = 0.216$ the structure only changed slightly from that shown in Fig. 7. Since in these cases significant wall slip took place and the microstructure was not distorted much further.

Despite the straining of the system, there was no significant change in the shape of the distribution of the contact number per particle with increasing strain, shown in Fig. 8(A). Therefore, the average contact numbers $\langle Z \rangle \sim 9$ remained nearly the same for the low strains applied in these experiments. However, $\langle Z \rangle$ was slightly higher for shear deformation $\gamma = 0.093$ compared to the sample before shear, $\gamma = 0$. The reason is perhaps the compression of the shells along the Z axis of the microscope during the relaxation of the bottom cassette creating slightly more contacts along Z. From the small amount the sample was strained in the experiment it is likely that shells did not significantly make or lose contacts during shear. Particles also hardly underwent rearrangements for the low applied shear deformation. This was also confirmed in the confocal movies taken during shear.

2. Contact forces

The calculated average contact forces and the respective relative standard deviations obtained from the sample subjected to shear are shown in Table I. We measured a 7% increase in the magnitude of the average force when the sample was deformed by an amount $\gamma = 0.093$ and for further strains the average force remained more or less the same. This increase in the average force during shear 1, perhaps resulted from the compression of the shells along the gradient direction during the relaxation of the bottom cassette. Further shear
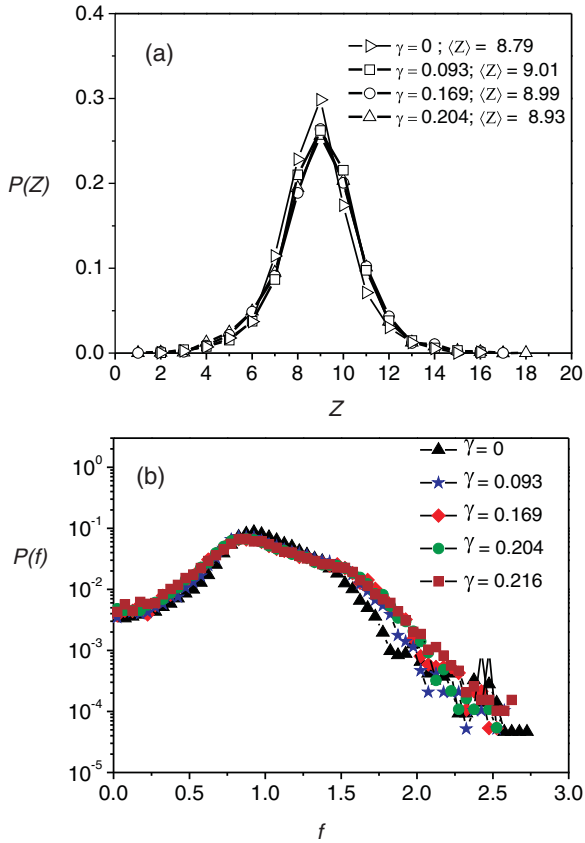
FIG. 8. Probability distribution of (a) contact number and (b) contact force normalized by the average contact force, per particle before shearing the sample and after the sample had been strained at different strain amplitudes.

apparently did not change the average contact forces for the small shear strains but the relative standard deviation $(\sigma_F/\langle F \rangle)$ increased slightly with increasing strain. This is perhaps not surprising, as shear deformation causes both a compression and an extension. Therefore, the probability distributions of the contact force magnitudes normalized by the average force, $P(f)$ became slightly wider with an increase in the measured strain from $\gamma = 0$ to $\gamma = 0.216$, as is seen in Fig. 8(b). The higher probability of large and small forces resulted from an increase in the deformations of approaching shells along the compression axis and a relaxation of shells receding along the extension axis. A similar broadening of the distribution under shear has been reported in granular materials where the tail of the distribution became less steep than exponential with applied shear [8]. However, this result is not consistent with the tail of distributions measured in a study by Corwin *et al.* [67], where the tail became steeper when the grains started to flow. To further investigate if the observed changes in the shape of the force distributions indeed correlate with the compression or extension axes of the shear we now turn to the angular distribution of the contact forces.

Shear-induced anisotropy in the orientation of the contact forces was analyzed by plotting the angle that the contacts make with the velocity axis for all forces with a magnitude above the average. Only the component of the force in the XZ plane was taken for the angle distribution. This distribution was

found to be anisotropic even before the sample was sheared, clearly showing the compression that was caused by lowering the upper plate onto the sample [Fig. 9(a)]. With the applied shear strain we noticed a clear increase in the probability in the quadrants 90°–180° and 270°–360°(compression zone) and a decrease of P(θ) in the other two quadrants (extension zone). The effect of shear becomes more clear in Fig. 9(b) where the ratio is plotted of the probability distribution after shear and before shear. Clearly, a significant increase in the probability of larger forces takes place between 135° and 170° with a maximum around 160°. A correspondingly large reduction is found between 10° and 45°, with a maximum at 20°. While these directions qualitatively correlate with the compression and extension axes of the shear there is a clear preference for a force build up at a smaller angles of around 20° to the velocity direction. A 3D visualization of the shear-induced anisotropic network of the contacts carrying larger forces (greater than 1.5 times average value) is depicted in Figs. 9(d) and 9(e), before and after shear. At $\gamma = 0$, larger forces in the force network are mostly aligned along the gradient axis in layers due to the compression induced by the plate-plate confinement. Upon shear the number of the force segments increased due to a build up of larger forces in the compression zone. However, the effect of the shear appears to consists of only a very small increase in the average length and persistence length of force chains [Fig. 9(c)] (Table S2 [56]), probably due to the small applied strain. Although the chain correlation is small, it is still higher compared to the static packings of shells at high volume fractions, where the samples were not confined between plates but the contact network was anisotropic. This result confirms the higher tendency for the forces to form linear chains under anisotropically applied stress, for example, shear.

Finally, a number of preliminary experiments with a larger strain were also conducted. This was possible only in a few cases where wall slip was almost absent using fresh glass plates. These successful results do indicate that a significantly larger strain can be applied without slip, in future work. Figure 10 shows the confocal images (XZ mode) of the amorphous packing of jammed shells taken after shearing the shells by an amount $\gamma = 1.72$ and $\gamma = 2.17$. The two images were taken from different experiments and the applied shear rates were $\dot{\gamma} = 7.8 \times 10^{-2} \ s^{-1}$ and $\dot{\gamma} = 2.8 \times 10^{-3} \ s^{-1}$. We didn't perform a quantitative analysis on these systems, but the observations revealed that these deeply jammed shells at these relatively large strains and shear rates do undergo fracture. In Figs. 10(a) and 10(b) cracks that developed during the strain in the sample can be seen along the direction approximately normal to the direction of extension. The formation of cracks is a likely indication that these packings behaved like a brittle amorphous solid under this shear rate and much larger strains than in the other experiments that were analyzed more quantitatively.

IV. CONCLUSIONS

In this article we have shown, by accurately measuring the interparticle forces, how elastic shells can serve as local force sensors in jammed states for a wide range of volume fractions above the jamming point. From the deflection of the shells at the contact points, we determined the magnitudes of the
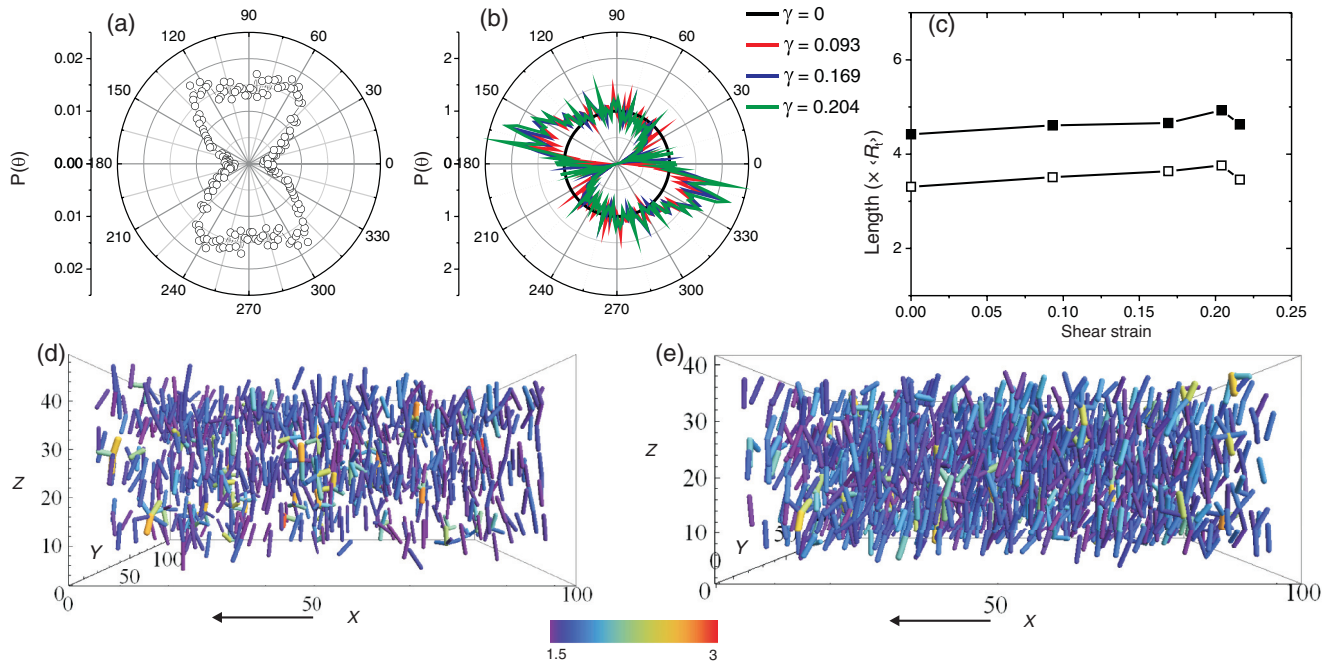
FIG. 9. (a) Probability distribution of the angle of contacts carrying forces above the average force with respect to the velocity direction (X axis) for $\gamma = 0$. (b) The ratio is plotted of the probability distribution after shear and before shear for three values of strain amplitudes. (c) The variation in average chain length (closed square) and persistence length (open square) of force chains obtained from shell packings shear. Force networks in jammed shells (d) before shear, $\gamma = 0$ and (e) after shear, $\gamma = 0.169$. for forces greater than 1.5 times the average value. The Z coordinate is increased by a factor of 1.5 for better visibility.

normal forces by a semiempirical force law that interpolates smoothly between linear and square root behavior. We found that with increasing compression, the probability distribution at larger forces changed from exponential near the jamming transition to Gaussian at higher packing densities. An analysis of the correlation between the contact forces did not produce evidence for the presence of a significant amount of force chains, though the forces were slightly anisotropic in the system due to the unidirectional compression in the preparation of the sample. Local correlations were slightly higher in the shear experiments. Although the shear deformations investigated in this study were small ($\gamma \leqslant 0.216$), the microstructure and contact force network showed already a pronounced

FIG. 10. Confocal images in XZ mode of jammed shells in two different preliminary experiments, under various amounts of shear at much larger shear strain and shear rate than in the experiments that were analyzed quantitatively in this paper. The systems underwent failure by developing cracks, in regions marked by the red ellipses (a) at a shear strain $\gamma = 1.72$ and shear rate $\dot{\gamma} = 7.8 \times 10^{-2}$ s^{-1} and (b) at a shear strain $\gamma = 2.17$ and shear rate $\dot{\gamma} = 2.8 \times 10^{-3}$ s^{-1}.

anisotropy with increasing strain. We observed an increase in the probability of forces both larger and smaller than average, which correlated with the compression and extension axes of the shear, respectively. Interestingly, the largest changes in the contact forces were seen not at $\pm 45°$ to the velocity axis but at $\pm 20°$. However, due to the small strains, no appreciable change was observed in the distribution of contact number. This reflected the fact that rearrangements of particles were almost absent. Apparently, the system was only elastically deformed by the applied stress. It would be interesting to carry out quantitative studies at higher values of strain, after introducing a better adhesion between the shells and the walls. Future studies therefore would involve a systematic investigation of mechanical and geometrical properties under applied shear (without slipping) at different volume fractions including marginally jammed shells. Moreover, research in the direction of the effects of friction, stiffness, polydispersity, shape anisotropy on jamming behavior, are also a possibility to address without too many modifications of the same model system as used in the present work.
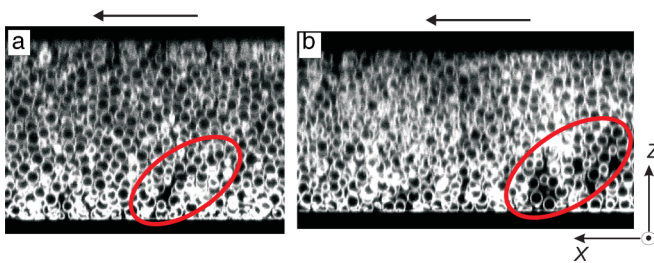
[1] C. H. Liu, S. R. Nagel, D. A. Schecter, S. N. Coppersmith, S. Majumdar, O. Narayan, and T. A. Witten, Science **269**, 513 (1995).

[2] H. M. Jaeger, S. R. Nagel, and R. P. Behringer, Rev. Mod. Phys. **68**, 1259 (1996).

[3] M. E. Cates, J. P. Wittmer, J. P. Bouchaud, and P. Claudin, Phys. Rev. Lett. **81**, 1841 (1998).

[4] D. M. Mueth, H. M. Jaeger, and S. R. Nagel, Phys. Rev. E **57**, 3164 (1998).

[5] D. L. Blair, N. W. Mueggenburg, A. H. Marshall, H. M. Jaeger, and S. R. Nagel, Phys. Rev. E **63**, 041304 (2001).

[6] J. M. Erikson, N. W. Mueggenburg, H. M. Jaeger, and S. R. Nagel, Phys. Rev. E **66**, 040301 (2002).

[7] G. Løvoll, K. J. Måløy, and E. G. Flekkøy, Phys. Rev. E **60**, 5872 (1999).

[8] T. S. Majmudar and R. P. Behringer, Nature (London) **435**, 1079 (2005).

[9] L. D. Landau and E. M. Lifshitz, *Theory of Elasticity* (Pergamon, New York, 1986).

[10] T. S. Majmudar, M. Sperl, S. Luding, and R. P. Behringer, Phys. Rev. Lett. **98**, 058001 (2007).

[11] G. Katgert and M. van Hecke, Europhys. Lett. **92**, 34002 (2010).

[12] J. Brujić, S. F. Edwards, I. Hopkinson, and H. A. Makse, Phys. A **327**, 201 (2003).

[13] J. Brujić, S. F. Edwards, D. V. Grinev, I. Hopkinson, D. Brujić, and H. A. Makse, Faraday Discuss. **123**, 207 (2003).

[14] J. Zhou, S. Long, Q. Wang, and A. D. Dinsmore, Science **312**, 1631 (2006).

[15] K. W. Desmond, P. J. Young, D. D. Chen, and E. R. Weeks, Soft Matter **9**, 3424 (2013).

[16] T. A. Caswell, Z. Zhang, M. L. Gardel, and S. R. Nagel, Phys. Rev. E **87**, 012303 (2013).

[17] D. W. Howell, R. P. Behringer, and C. T. Veje, Chaos **9**, 559 (1999).

[18] C. S. O'Hern, S. A. Langer, A. J. Liu, and S. R. Nagel, Phys. Rev. Lett. **86**, 111 (2001).

[19] C. S. O'Hern, S. A. Langer, A. J. Liu, and S. R. Nagel, Phys. Rev. Lett. **88**, 075507 (2002).

[20] C. S. O'Hern, L. E. Silbert, A. J. Liu, and S. R. Nagel, Phys. Rev. E **68**, 011306 (2003).

[21] H. A. Makse, D. L. Johnson, and L. M. Schwartz, Phys. Rev. Lett. **84**, 4160 (2000).

[22] H. P. Zhang and H. A. Makse, Phys. Rev. E **72**, 011301 (2005).

[23] M. van Hecke, Nature (London) **435**, 1041 (2005).

[24] S. Ostojic, T. J. H. Vlugt, and B. Nienhuis, Phys. Rev. E **75**, 030301 (2007).

[25] J. H. Snoeijer, W. G. Ellenbroek, T. J. H. Vlugt, and M. van Hecke, Phys. Rev. Lett. **96**, 098001 (2006).

[26] F. Radjai, D. E. Wolf, M. Jean, and J. J. Moreau, Phys. Rev. Lett. **80**, 61 (1998).

[27] J. Geng, G. Reydellet, E. Clément, and R. P. Behringer, Phys. D **182**, 274 (2003).

[28] D. Bi, J. Zhang, B. Chakraborty, and R. P. Behringer, Nature (London) **480**, 355 (2011).

[29] J. Jose, G. A. Blab, A. van Blaaderen, and A. Imhof, Soft Matter **11**, 1800 (2015).

[30] N. A. Elbers, J. Jose, A. Imhof, and A. van Blaaderen, Chem. Mater. **27**, 1709 (2015).

[31] C. I. Zoldesi, I. L. Ivanovska, C. Quilliet, G. J. L. Wuite, and A. Imhof, Phys. Rev. E **78**, 051401 (2008).

[32] J. Jose, M. Kamp, A. van Blaaderen, and A. Imhof, Langmuir **30**, 2385 (2014).

[33] M. van Hecke, J. Phys.: Condens. Matter **22**, 033101 (2010).

[34] A. J. Liu and S. R. Nagel, Annu. Rev. Condens. Matter Phys. **1**, 347 (2010).

[35] H. M. Jaeger, Soft Matter **11**, 12 (2015).

[36] F. Caruso, Adv. Mater. **13**, 11 (2001).

[37] S. L. Westcott, S. J. Oldenburg, T. R. Lee, and N. J. Halas, Langmuir **14**, 5396 (1998).

[38] C. I. Zoldesi and A. Imhof, Adv. Mater. **17**, 924 (2005).

[39] C. I. Zoldesi, C. A. van Walree, and A. Imhof, Langmuir **22**, 4343 (2006).

[40] A. Baule and H. A. Makse, Soft Matter **10**, 4423 (2014).

[41] H. F. Burcharth, K. d'Angremond, J. W. Van der Meer, and Z. Liu, Coastal Engineering **40**, 183 (2000).

[42] S. Remond, J. L. Gallias, and A. Mizrahi, Granular Matter **10**, 157 (2008).

[43] L. N. Zou, X. Cheng, M. L. Rivers, H. M. Jaeger, and S. R. Nagel, Science **326**, 408 (2009).

[44] S. A. Galindo-Torres, F. Alonso-Marroquín, Y. C. Wang, D. Pedroso, and J. D. Muñoz Castaño, Phys. Rev. E **79**, 060301(R) (2009).

[45] I. Malinouskaya, V. V. Mourzenko, J. F. Thovert, and P. M. Adler, Phys. Rev. E **80**, 011304 (2009).

[46] C. S. Peyratout and L. Dahne, Angew. Chem. Int. Ed. **43**, 3762 (2004).

[47] A. P. R. Johnston, C. Cortez, A. S. Angelatos, and F. Caruso, Curr. Opin. Colloid Interface Sci. **11**, 203 (2006).

[48] K. Ariga, J. P. Hill, M. V. Lee, A. Vinu, R. Charvet, and S. Acharya, Sci. Technol. Adv. Mater. **9**, 1 (2008).

[49] D. M. Vriezema, M. C. Aragones, J. Elemans, J. Cornelissen, A. E. Rowan, and R. J. M. Nolte, Chem. Rev. **105**, 1445 (2005).

[50] H. N. Yow and A. F. Routh, Soft Matter **2**, 940 (2006).

[51] F. Caruso, Chem. Eur. J. **6**, 413 (2000).

[52] L. Zhang, M. DAcunzi, M. Kappl, G. K. Auernhammer, D. Vollmer, C. M. van Kats, and A. van Blaaderen, Langmuir **25**, 2711 (2009).

[53] D. J. Durian, Phys. Rev. Lett. **75**, 4780 (1995).

[54] Z. Zhang, N. Xu, D. T. N. Chen, P. Yunker, A. M. Alsayed, K. B. Aptowicz, P. Habdas, A. J. Liu, S. R. Nagel, and A. G. Yodh, Nature (London) **459**, 230 (2009).

[55] A. V. Pogorelov, *Bendings of Surfaces and Stability of Shells* (American Mathematical Society, Providence, RI, 1988).

[56] See Supplemental Material at http://link.aps.org/supplemental/10.1103/PhysRevE.93.062901 for details on the samples, the validation of the force law, and the characterization of the force network.

[57] Y. L. Wu, J. H. J. Brand, J. L. A. van Gemert, J. Verkerk, H. Wisman, A. van Blaaderen, and A. Imhof, Rev. Sci. Instrum. **78**, 103902 (2007).

[58] T. H. Besseling, J. Jose, and A. van Blaaderen, J. Microsc. **257**, 142 (2015).

[59] S. Hell, G. Reiner, C. Cremer, and E. H. K. Stelzer, J. Microsc. **169**, 391 (1993).

[60] E. Reissner, J. Math. Phys. **25**, 80 (1946).

[61] E. Reissner, J. Math. Phys. **25**, 279 (1946).

[62] A. Fery, F. Dubreuil, and H. Möhwald, New J. Phys. **6**, 18 (2004).

[63] V. V. Lulevich, D. Andrienko, and O. I. Vinogradova, J. Chem. Phys. **120**, 3822 (2004).

[64] M. Wyart, L. E. Silbert, S. R. Nagel, and T. A. Witten, Phys. Rev. E **72**, 051306 (2005).

[65] I. Jorjadze, L. L. Pontani, and J. Brujić, Phys. Rev. Lett. **110**, 048302 (2013).

[66] W. G. Ellenbroek, Z. Zeravcic, W. van Saarloos, and M. van Hecke, Europhys. Lett. **87**, 34004 (2009).

[67] E. I. Corwin, H. M. Jaeger, and S. R. Nagel, Nature (London) **435**, 1075 (2005).